A smoothed finite element method using second-order cone programming

Jingjing Meng[1], Xue Zhang[2,3*], Jinsong Huang[4], Hongxiang Tang[3], Hans Mattsson[1], Jan Laue[1]

1. Department of Civil, Environmental and Natural Resources Engineering, Luleå University of Technology, Luleå, Sweden
2. Department of Civil Engineering and Industrial Design, University of Liverpool, Liverpool, United Kingdom
3. State Key Laboratory of Coastal and Offshore Engineering, Dalian University of Technology, China
4. Discipline of Civil, Surveying & Environmental Engineering, Priority Research Centre for Geotechnical Science & Engineering, The University of Newcastle, Callaghan, NSW 2308, Australia

Abstract

In this paper, a new approach abbreviated as SOCP-SFEM is developed for analysing geomechanical problems in elastoplasticity. The SOCP-SFEM combines a strain smoothing technique with the finite element method (FEM) in second-order cone programming (SOCP) and thereby inherits the advantages of both the smoothed finite element method (SFEM) and the SOCP-FEM. Specifically, the low-order mixed element can be used in the SOCP-SFEM without volumetric locking issues and the singularity associated with some typical constitutive models (e.g. the Mohr-Coulomb model and the Drucker-Prager model) is no longer a problem. In addition, the frictional and the cohesive-frictional interfaces can be implemented straightforward in the developed SOCP-SFEM owing to the adopted mixed variational principle and the smoothing technique. Furthermore, the multiple contact constraints, such as a cohesive interface with tension cut-off which is commonly used for analysing the bearing capacity of a pipeline buried in clays, can be simulated with little extra efforts. To verify the correctness and robustness of the developed formulation for SOCP-SFEM, a series of benchmarks are considered where the simulation results are in good agreements with the analytical solutions and the reported numerical results.

Keywords: Smoothed finite element method, Convex programming, Strain smoothing technique, Second-order cone programming, Contact problems

----

* Email address: xue.zhang2@liverpool.ac.uk

1. Introduction

The classic finite element method (FEM) is typically developed in a nested solution manner based on the Newton–Raphson iteration [1]. In each time increment, the state variables (e.g., displacements and stresses) are calculated through iteration loops of elastic prediction and plastic correction between global structural levels, where out-of-balance forces are minimised using Newton's method or its variants [2, 3], and local material levels (i.e. Gauss integration points) where stress-strain relationships are fulfilled.

An alternative to the nested algorithm is the FEM in mathematical programming [4]. In addition to the wide applications of computational limit analysis of solids [5-8], the FEM in mathematical programming has been demonstrated to be a powerful technique in dealing with complex geomechanical problems. An attractive feature associated with the FEM in mathematical programming lies in the fact that it allows for mathematical analysis of the existence, uniqueness, and sensitivity of the resulting optimisation problem [1, 9, 10]. Additionally, the implementation is not an issue. Once the developed formulations are cast into a particular type of optimisation problems, modern optimisation solvers are available which releases the researchers from designing and programming the solution algorithm. Among different versions of the FEM in mathematical programming, the FEM in second-order cone programming (SOCP) is perhaps the one that has attracted most attentions in the past decades or so. This is to a large extent owing to some unique merits associated with the FEM in SOCP (SOCP-FEM) for computational plasticity. The widely used constitutive models for solids and fluids such as the Mohr-Coulomb model, the Drucker Prager model and the Bingham model can be naturally cast into second-order conic constraints in the SOCP-FEM, which means singularities in the yield surfaces of these models are no longer problems [11, 12]. Additionally, the extension from single-surface plasticity to multi-surface plasticity in the

SOCP-FEM can be achieved by simply including conic constraints in the resulting optimisation problem requiring little extra efforts. Furthermore, very efficient off-the-shelf SOCP solvers, such as MOSEK [13] and SeDuMi [14], have been developed in the last decade or so implying that large-scale problems can be tackled efficiently. Consequently, numerous efforts have so far been dedicated to reformulating various nonlinear mechanics problems as a SOCP program which include, but are not limited to, static analysis of elastoplastic problems [11, 15, 16], analysis of steady-state yield flows fluid [17, 18], consolidation analysis of saturated porous media [19], progressive failure analysis of sensitive clays [10, 20], granular contact dynamics [21-24], particle finite element analysis [25-27], discontinuous deformation analysis [28-30], stability analysis of masonry block structures [31, 32] and rock failure behaviour [33, 34].

It is notable that the SOCP-FEM [25, 35] still encounters the volumetric locking problem [36] if linear mixed triangular elements are used even though it is developed on the mixed variational principle. To overcome this issue, a strain smoothing technique [36, 37] developed in the smoothed finite element method (SFEM) [36, 38, 39] is implemented in the framework of the SOCP-FEM in this paper. The basic idea is that the strain smoothing is performed over the smoothing domains that are constructed based on finite elements and the global system of equations are generated on smoothing domains rather than on finite elements to solve the unknowns. In this paper, the node-based smoothing domain is used and implemented in the SOCP-FEM owing to its following properties [38, 39]: upper bound in the strain energy of the exact solution when a reasonably fine mesh is used; super-accurate and super-convergent properties of stress solutions; usage of an arbitrary number of sides of polygonal elements and insensitivity to element distortion. It is shown that, as a mixture of the SOCP-FEM and the SFEM, the newly developed approach (abbreviated as SOCP-SFEM) inherits the advantages of both approaches and, furthermore, offers a more straightforward way of coping with cohesive-frictional interfaces.

The paper is organised as follows. In Section 2, we present strain smoothing technique of the SFEM before proposing the variational formulation of the SOCP-SFEM in Section 3. In Section 4, the procedures of converting the resulting problems into a standard SOCP program are demonstrated. In section 5, the proposed approach is validated with four benchmarks, in which the calculated numerical results are compared with analytical solution and reported numerical results before conclusions are drawn in Section 6.

2. Principle of smoothed finite element method

2.1 Creation of node-based smoothing domains

The SFEM starts with creating smoothing domains associated with FEM nodes based on given FEM meshes. An illustration of the generation of "non-overlap" and "no-gap" smoothing domains for the node-based SFEM is shown in Fig.1. As depicted, the smoothing domain Ω_k^s assigned to node *k* is the coloured polygon covering one-third of all the node's adjacent elements. The smoothing domain is bounded by multiple straight boundary segments which connect the midpoint of an element edge to a centroid of a triangular element. In the SFEM, the operation of strain smoothing is carried out on these smoothing domains instead of finite elements.

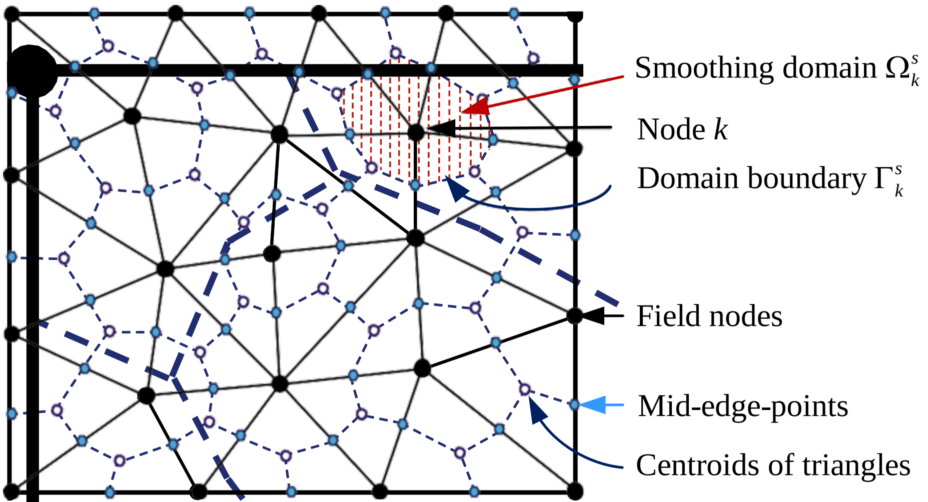

Fig. 1. An illustration of node-based smoothing domains created based on FEM meshes (after [36]). The FEM meshes are represented by solid black lines.

2.2 Strain smoothing technique

Following the classic FEM, for each finite element the strain-displacement relation is given as:

$$\boldsymbol{\varepsilon} = \mathbf{B}_{\mathrm{u}}\hat{\mathbf{u}} \tag{1}$$

where $\boldsymbol{\varepsilon}$ is the strain field that is uniform within the element because the three-node triangular element is adopted, $\mathbf{B}_{\mathrm{u}}$ is the strain-displacement matrix and $\hat{\mathbf{u}}$ is a vector consisting of nodal displacements.

In the smoothing domain Ω_k^s (Fig.1), the smoothed strain $\bar{\boldsymbol{\varepsilon}}_k$ at node k is calculated by:

$$\bar{\boldsymbol{\varepsilon}}_k = \int_{\Omega_k^s} \Phi_k(\mathbf{x})\varepsilon(\mathbf{x})\mathrm{d}\Omega = \int_{\Omega_k^s} \Phi_k(\mathbf{x})\mathbf{B}_{\mathrm{u}}\hat{\mathbf{u}}\mathrm{d}\Omega \tag{2}$$

where $\Phi_k(\mathbf{x})$ is the smoothing function and, in this study, the local constant smoothing function [37, 40]

$$\Phi_k(\mathbf{x}) = \begin{cases} 1/\mathrm{A}_k^s, & \mathbf{x} \in \Omega_k^s \\ 0, & \mathbf{x} \notin \Omega_k^s \end{cases} \tag{3}$$

is used where A_k^s is the area of the smoothing domain Ω_k^s.

As demonstrated in Fig.1, the smoothing domain Ω_k^s is comprised of N_s sub-smoothing domains which are one-third of the FEM triangular elements. Since the strain is uniform inside the adopted linear triangular element, the smoothed strain $\bar{\boldsymbol{\varepsilon}}_k$ is:

$$\bar{\boldsymbol{\varepsilon}}_k = \frac{1}{\mathrm{A}_k^s}\sum_{i=1}^{N_s}\frac{1}{3}\mathrm{A}_i^e\boldsymbol{\varepsilon}_i^e = \frac{1}{\mathrm{A}_k^s}\sum_{i=1}^{N_s}\frac{1}{3}\mathrm{A}_i^e\mathbf{B}_i^e\hat{\mathbf{u}}_i^e \tag{4}$$

where A_i^e, $\boldsymbol{\varepsilon}_i^e$, $\mathbf{B}_i^e$ and $\hat{\mathbf{u}}_i^e$ are the area, the strain, the strain gradient matrix and the displacement of the *i*th triangular element, respectively. In brief, the basic idea of the node-based SFEM lies in the calculation of a smoothed uniform strain (4) for each supporting domain based on the displacement of finite element nodes. The strain at the supporting domain is influenced by nodal displacements of all the finite elements that cover the supporting domain.

3. Second-order cone programming formulation of smoothed finite element method

3.1 Hellinger-Reissner Variational Principle

Differing from the principle of minimum potential energy in which displacements are the only basic variables, Hellinger-Reissner variational principle regards both the displacements and the stresses as independent master fields [41]. For an elastostatic boundary-value problem, the Hellinger-Reissner functional reads:

$$\Pi(\boldsymbol{\sigma},\mathbf{u}) = \int_\Omega \boldsymbol{\sigma}^{\mathrm{T}}\nabla\boldsymbol{u}\,\mathrm{d}\Omega - \int_\Omega \mathbf{b}^{\mathrm{T}}\mathbf{u}\,\mathrm{d}\Omega - \int_\Gamma \mathbf{t}^{\mathrm{T}}\mathbf{u}\,\mathrm{d}\Omega - \int_\Omega \frac{1}{2}\boldsymbol{\sigma}^{\mathrm{T}}\mathbb{C}\boldsymbol{\sigma}\,\mathrm{d}\Omega \tag{5}$$

where $\boldsymbol{\sigma}$ is the stress, $\mathbf{b}$ is the body force, $\mathbf{t}$ is the traction, ∇ is the usual linear strain-displacement differential operator and $\mathbb{C}$ is the elastic compliance modulus. In plane-strain cases, the elastic compliance modulus is

$$\mathbb{C} = \frac{1+\upsilon}{E}\begin{bmatrix} 1-\upsilon & -\upsilon & 0 \\ -\upsilon & 1-\upsilon & 0 \\ 0 & 0 & 2 \end{bmatrix} \tag{6}$$

where E and υ are the elastic modulus and Poisson's ratio, respectively.

The solution of the boundary-value problem can be obtained via $\delta\Pi(\boldsymbol{\sigma},\mathbf{u})=0$ and the obtained solution is a saddle point of the functional. In other words, the elastostatic boundary-value problem is equivalent to the following min-max optimisation problem [19]:

$$\min_{\mathbf{u}}\ \max_{\boldsymbol{\sigma}}\ \int_{\Omega}\boldsymbol{\sigma}^{\mathrm{T}}\nabla\mathbf{u}\mathrm{d}\Omega-\int_{\Omega}\mathbf{b}^{\mathrm{T}}\mathbf{u}\mathrm{d}\Omega-\int_{\Gamma}\mathbf{t}^{\mathrm{T}}\mathbf{u}\mathrm{d}\Omega-\int_{\Omega}\frac{1}{2}\boldsymbol{\sigma}^{\mathrm{T}}\mathbb{C}\boldsymbol{\sigma}\mathrm{d}\Omega \tag{7}$$

The extension of the above min-max problem to incremental elastoplastic analysis is straightforward. It can be achieved by expressing the incremental form with a yield condition being included as a constraint:

$$\begin{aligned}&\min_{\Delta\mathbf{u}}\ \max_{\boldsymbol{\sigma}_{\mathrm{n+1}}}\ \int_{\Omega}\boldsymbol{\sigma}_{\mathrm{n+1}}^{\mathrm{T}}\nabla\left(\Delta\mathbf{u}\right)\mathrm{d}\Omega-\int_{\Omega}\mathbf{b}^{\mathrm{T}}\left(\Delta\mathbf{u}\right)\mathrm{d}\Omega-\int_{\Gamma}\mathbf{t}^{\mathrm{T}}\left(\Delta\mathbf{u}\right)\mathrm{d}\Omega-\int_{\Omega}\frac{1}{2}\left(\Delta\boldsymbol{\sigma}\right)^{\mathrm{T}}\mathbb{C}\left(\Delta\boldsymbol{\sigma}\right)\mathrm{d}\Omega\\&\text{subject to }\ F\left(\boldsymbol{\sigma}_{n+1}\right)\le 0\end{aligned} \tag{8}$$

where the displacement and stress increments are $\Delta\mathbf{u}=\mathbf{u}_{\mathrm{n+1}}-\mathbf{u}_{\mathrm{n}}$ and $\Delta\boldsymbol{\sigma}=\boldsymbol{\sigma}_{\mathrm{n+1}}-\boldsymbol{\sigma}_{\mathrm{n}}$, respectively, and *F* is the yield function. The subscripts n+1 and n denote the unknown and known states of the corresponding variables.

3.2 Optimality conditions

To prove its validity, the optimality conditions of problem (8) are derived in this section. Following the procedure in [42-44], the inequality constraint is converted into an equality constraint by introducing a positive slack variable *s*. To enforce the constraint *s*≥0 explicitly, a logarithmic barrier function is included in the objective function. Problem (8) thereby is reformulated as

$$\begin{aligned}&\min_{\Delta\mathbf{u}}\ \max_{\boldsymbol{\sigma}_{\mathrm{n+1}}}\ \int_{\Omega}\boldsymbol{\sigma}_{\mathrm{n+1}}^{\mathrm{T}}\nabla\left(\Delta\mathbf{u}\right)\mathrm{d}\Omega-\int_{\Omega}\mathbf{b}^{\mathrm{T}}\left(\Delta\mathbf{u}\right)\mathrm{d}\Omega-\int_{\Gamma}\mathbf{t}^{\mathrm{T}}\left(\Delta\mathbf{u}\right)\mathrm{d}\Omega-\int_{\Omega}\frac{1}{2}\left(\Delta\boldsymbol{\sigma}\right)^{\mathrm{T}}\mathbb{C}\left(\Delta\boldsymbol{\sigma}\right)\mathrm{d}\Omega+\beta\ln s\\&\text{subject to }\ F\left(\boldsymbol{\sigma}_{\mathrm{n+1}}\right)+s=0\end{aligned} \tag{9}$$

where β is an arbitrarily small positive constant. The standard Lagrange multiplier technique can be employed to solve (9) by first constructing its associated Lagrangian

$$\begin{aligned}\mathrm{L}=&\int_{\Omega}\boldsymbol{\sigma}_{\mathrm{n+1}}^{\mathrm{T}}\nabla\left(\Delta\mathbf{u}\right)\mathrm{d}\Omega-\int_{\Omega}\mathbf{b}^{\mathrm{T}}\left(\Delta\mathbf{u}\right)\mathrm{d}\Omega-\int_{\Gamma}\mathbf{t}^{\mathrm{T}}\left(\Delta\mathbf{u}\right)\mathrm{d}\Omega-\int_{\Omega}\frac{1}{2}\left(\Delta\boldsymbol{\sigma}\right)^{\mathrm{T}}\mathbb{C}\left(\Delta\boldsymbol{\sigma}\right)\mathrm{d}\Omega\\&+\int_{\Omega}\beta\ln s\mathrm{d}\Omega-\int_{\Omega}\Delta\lambda(F\left(\boldsymbol{\sigma}_{\mathrm{n+1}}\right)+s)\mathrm{d}\Omega\end{aligned} \tag{10}$$

where λ is the Lagrangian multiplier. The optimality conditions associated with problem (9) are then derived by the differentiation of (10) which results in the following set of governing equations:

$$\frac{\partial\mathrm{L}}{\partial\left(\Delta\mathbf{u}\right)}=\begin{cases}\nabla^{\mathrm{T}}\boldsymbol{\sigma}_{n+1}+\boldsymbol{b}=\mathbf{0}, & \text{in } \Omega\\ \mathbf{N}^{\mathrm{T}}\boldsymbol{\sigma}_{n+1}=\boldsymbol{t}, & \text{on } \Gamma\end{cases} \tag{11}$$

where $\mathbf{N}$ is the matrix containing the unit outward normal to the boundary Γ;

$$\frac{\partial\mathrm{L}}{\partial\boldsymbol{\sigma}_{\mathrm{n+1}}}=\nabla\left(\Delta\mathbf{u}\right)-\mathbb{C}\Delta\boldsymbol{\sigma}-\Delta\lambda\frac{\partial F}{\partial\boldsymbol{\sigma}_{\mathrm{n+1}}}=0 \tag{12}$$

$$\frac{\partial\mathrm{L}}{\partial\Delta\lambda}=F\left(\boldsymbol{\sigma}_{\mathrm{n+1}}\right)+s=0 \tag{13}$$

$$\frac{\partial\mathrm{L}}{\partial s}=\frac{\beta}{s}-\Delta\lambda=0\Rightarrow\beta=s\Delta\lambda \tag{14}$$

Obviously, Eq. (11) reproduces the equilibrium equation and the boundary condition and Eq. (12) states that the total strain increment $\Delta\boldsymbol{\varepsilon}$ is split into an elastic part $\Delta\boldsymbol{\varepsilon}^{\mathrm{e}}$ and a plastic part $\Delta\boldsymbol{\varepsilon}^{\mathrm{p}}$ by additive decomposition as:

$$\nabla\left(\Delta\mathbf{u}\right)=\Delta\boldsymbol{\varepsilon}=\Delta\boldsymbol{\varepsilon}^{\mathrm{e}}+\Delta\boldsymbol{\varepsilon}^{\mathrm{p}} \tag{15}$$

where

$$\begin{cases} \Delta\boldsymbol{\varepsilon}^{\mathrm{e}} = \mathbb{C}\Delta\boldsymbol{\sigma} \\ \Delta\boldsymbol{\varepsilon}^{\mathrm{p}} = \Delta\lambda \dfrac{\partial F}{\partial \boldsymbol{\sigma}_{\mathrm{n+1}}} \end{cases} \tag{16}$$

Eq. (13) illustrates the yield function F recalling that s is a small positive variable. Eq. (14) (in the limit of β=0) ensures that plastic deformation takes place only when the stresses reach the yield surface and otherwise. It is clear that the derived optimality conditions associated with the min-max optimisation problem (9) are the governing equations for the quasi-static analysis in elastoplasticity. In order to use convex programming, the associated flow rule is adopted in this work. Therefore, the plastic potential is same to the yield function F.

3.3 Smoothed finite element discretisation

Using standard FEM notations, the displacement can be interpolated using shape functions as:

$$\mathbf{u} \approx \mathbf{N}_{\mathrm{u}}\hat{\mathbf{u}} \tag{17}$$

where $\hat{\mathbf{u}}$ is the nodal displacement vector of the element, $\mathbf{N}_{\mathrm{u}}$ is the matrix containing the shape functions for displacements arranged as:

$$\mathbf{N}_u = \begin{bmatrix} N_1 & 0 & N_2 & 0 & N_3 & 0 \\ 0 & N_1 & 0 & N_2 & 0 & N_3 \end{bmatrix} \tag{18}$$

with N_1, N_2 and N_3 being three shape functions corresponding to three nodes of the linear triangular element.

For the ith element, the strain-displacement matrix is $\mathbf{B}_i^e = \nabla \mathbf{N}_u$ and thereby is in the form of

$$\mathbf{B}_i^e = \begin{bmatrix} \frac{\partial N_1}{\partial x} & 0 & \frac{\partial N_2}{\partial x} & 0 & \frac{\partial N_3}{\partial x} & 0 \\ 0 & \frac{\partial N_1}{\partial y} & 0 & \frac{\partial N_2}{\partial y} & 0 & \frac{\partial N_3}{\partial y} \\ \frac{\partial N_1}{\partial y} & \frac{\partial N_1}{\partial x} & \frac{\partial N_2}{\partial y} & \frac{\partial N_2}{\partial x} & \frac{\partial N_3}{\partial y} & \frac{\partial N_3}{\partial x} \end{bmatrix} \tag{19}$$

Substituting (19) into (4) results in the smoothed strain $\bar{\boldsymbol{\varepsilon}}_k$ on the smoothing domain Ω_k^s, which is

$$\bar{\boldsymbol{\varepsilon}}_k = \bar{\mathbf{B}}_k \hat{\mathbf{u}}_k \tag{20}$$

where

$$\bar{\mathbf{B}}_k = \frac{1}{\mathrm{A}_k^s} \sum_{i=1}^{N_s} \frac{1}{3} \mathrm{A}_i^e \mathbf{B}_i^e \tag{21}$$

The following notation is used for the stress interpolation:

$$\boldsymbol{\sigma} \approx \mathbf{N}_\sigma \bar{\boldsymbol{\sigma}} \tag{22}$$

where $\bar{\boldsymbol{\sigma}}$ is the stress at the node which can also be interpreted as a smoothed stress of the smoothing domain (e.g. the stress at the *k*th node which is also the smoothed stress for the *k*th smoothing domain), and $\mathbf{N}_\sigma$ is the matrix containing the shape function for the stress. For the linear triangular elements, both the smoothed strains and stresses are uniform within the smoothing domains. Hence, the shape function matrix for stress (i.e. $\mathbf{N}_\sigma$) is simply an identity matrix.

The principle (8) is discretised in space by using Eqs. (17), (20) and (22), which is given as:

$$\begin{aligned} &\min_{\Delta\hat{\mathbf{u}}} \max_{\bar{\sigma}_{\mathrm{n+1}}} \quad \Delta\hat{\mathbf{u}}^{\mathrm{T}} \mathbf{B}^{\mathrm{T}} \bar{\boldsymbol{\sigma}}_{\mathrm{n+1}} - \Delta\hat{\mathbf{u}}^{\mathrm{T}} \tilde{\mathbf{f}} - \frac{1}{2} \Delta\bar{\boldsymbol{\sigma}}_{\mathrm{n+1}}^{\mathrm{T}} \mathbf{C} \Delta\bar{\boldsymbol{\sigma}}_{\mathrm{n+1}} \\ &\text{subject to } F\left(\bar{\boldsymbol{\sigma}}_{\mathrm{n+1}}\right) \le 0 \end{aligned} \tag{23}$$

where

$$\mathbf{B}^{\mathrm{T}} = \int_{\Omega_s} (\bar{\mathbf{B}}_k)^{\mathrm{T}} \mathbf{N}_\sigma \mathrm{d}\Omega, \ \mathbf{C} = \int_{\Omega_s} \mathbf{N}_\sigma^{\mathrm{T}} \mathbb{C} \mathbf{N}_\sigma \mathrm{d}\Omega \text{ and } \tilde{\mathbf{f}} = \int_{\Omega_s} \mathbf{N}_{\mathrm{u}}^{\mathrm{T}} \mathbf{b} \mathbf{N}_\sigma \mathrm{d}\Omega + \int_{\Gamma} \mathbf{N}_{\mathrm{u}}^{\mathrm{T}} \mathbf{t} \mathrm{d}\Gamma \tag{24}$$

It is notable that in the SFEM the integration is calculated on node-based smoothing domains Ω_s rather than on finite elements. Because the linear triangular elements are employed, the integration of equations in (24) can be performed analytically.

3.4 Frictional and cohesive-frictional interfaces

A proper treatment of interfaces between a solid body (e.g. cone penetrometers, pipelines, retaining walls) and soils in the numerical model is essential for analysing geotechnical problems. Inspired by the recently proposed framework for the discrete element method, the contact algorithm has been developed in the SOCP-FEM [25]. The effectiveness and efficiency of the algorithm have been demonstrated through a series of studies on large deformation problems, in which dynamic nonlinear contacts between rigid surfaces and deformable bodies occur often. However, the algorithm developed in [25] is restricted to the purely frictional contact. In this study, contact algorithms for both the purely frictional and the cohesive-frictional interfaces are developed in the SOCP-SFEM.

As indicated in Fig. 2, interfaces are considered for yellow smoothing domains which are in contact with the rigid surface while red smoothing domains have potential to contact the surface. To prevent the penetration of the deformable body into the rigid surface, the following non-penetration conditions are imposed:

$$\begin{aligned} g^I &= g_0^I + \left(\Delta\hat{\mathbf{u}}^I\right)^{\mathrm{T}} \boldsymbol{n}^I \geq 0 \\ p^I g^I &= 0 \end{aligned} \tag{25}$$

where $\Delta\hat{\mathbf{u}}^I$ is the displacement increment of the node at contact I, $\boldsymbol{n}^I$ is the outward normal vector of the boundary, p^I is the contact force from the boundary, g_0^I is the initial gap and g^I is the gap at the next step.

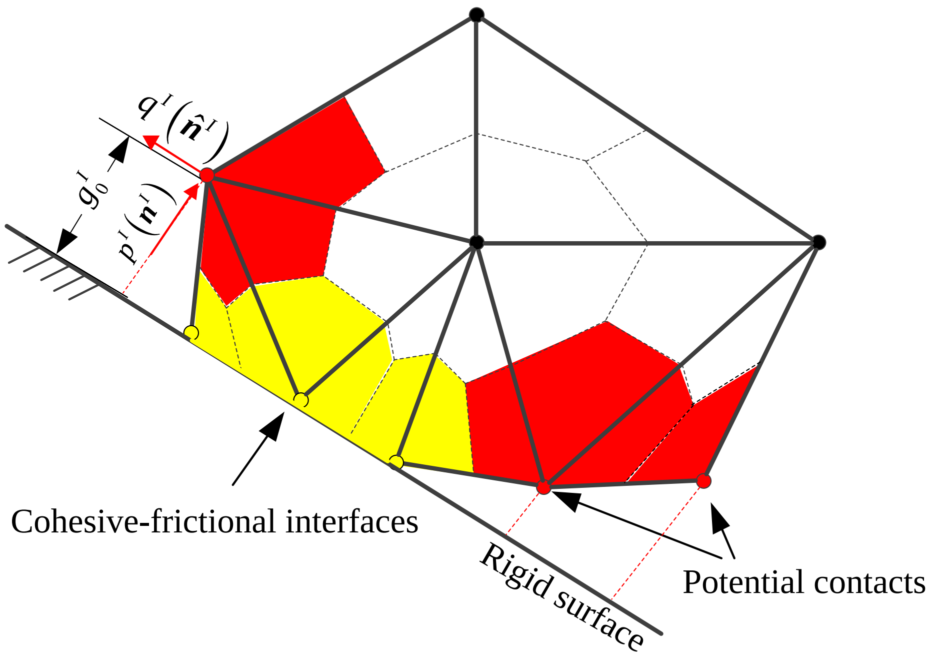

Fig. 2. Contacts between a deformable body and a rigid surface. Smoothing domains are shown with dash lines. Smoothing domains with cohesive-frictional interfaces are coloured in yellow. Red smoothing domains that have potential contacts are considered as purely frictional behaviour.

Following the approach in [23, 28, 33], the condition (25) can be enforced into the principle (23) leading to:

$$\begin{aligned}
&\min_{\Delta\hat{\mathbf{u}}}\ \max_{\bar{\boldsymbol{\sigma}}_{n+1}}\quad \Delta\hat{\mathbf{u}}^{\mathrm{T}}\mathbf{B}^{\mathrm{T}}\bar{\boldsymbol{\sigma}}_{n+1}-\Delta\hat{\mathbf{u}}^{\mathrm{T}}\tilde{\mathbf{f}}-\Delta\hat{\mathbf{u}}^{\mathrm{T}}\left(\boldsymbol{n}\boldsymbol{p}+\hat{\boldsymbol{n}}\boldsymbol{q}\right)-\frac{1}{2}\Delta\bar{\boldsymbol{\sigma}}_{n+1}^{\mathrm{T}}\mathbf{C}\Delta\bar{\boldsymbol{\sigma}}_{n+1}-\sum_{I=1}^{N_b} g_0^I p^I \\
&\text{subject to}\quad F\left(\bar{\boldsymbol{\sigma}}_{n+1}\right)\le 0 \\
&\qquad\qquad\quad\ F_b\left(\boldsymbol{p},\ \boldsymbol{q}\right)\le 0
\end{aligned} \tag{26}$$

where N_b is the number of boundary contacts, the normal and tangential vectors of the boundaries are collected in $\boldsymbol{n}$ and $\hat{\boldsymbol{n}}$, respectively, contact forces in the normal and tangential directions are organised into vectors $\boldsymbol{p}$ and $\boldsymbol{q}$, respectively, and shear strength for boundary contacts is considered with a constraint (i.e. $F_b\left(\boldsymbol{p},\ \boldsymbol{q}\right)\le 0$). The constraints on the shear strength for the boundary contact are formulated as:

$$\begin{cases} \left|\boldsymbol{q}\right| \le \mu \boldsymbol{p}, & \text{frictional interfaces} \\ \left|\boldsymbol{q}\right| \le \tan\phi\, \boldsymbol{p} + c\boldsymbol{A}, & \text{cohesive-frictional interfaces} \end{cases} \tag{27}$$

where μ is the friction coefficient, ϕ is the internal friction angle, c is the cohesion of the shear strength and A is the area of the interfaces.

The minimisation part of principle (27) with respect to $\Delta\hat{\mathbf{u}}$ can be solved analytically resulting in a maximisation problem:

$$\begin{aligned} \max_{\bar{\boldsymbol{\sigma}}_{\mathrm{n+1}},\,\boldsymbol{p},\,\boldsymbol{q}} \quad & -\frac{1}{2}\Delta\bar{\boldsymbol{\sigma}}_{\mathrm{n+1}}^{\mathrm{T}}\mathbf{C}\Delta\bar{\boldsymbol{\sigma}}_{\mathrm{n+1}} - \sum_{I=1}^{N_b} g_0^I p^I \\ \text{subject to} \quad & \mathbf{B}^{\mathrm{T}}\bar{\boldsymbol{\sigma}}_{\mathrm{n+1}} = \tilde{\mathbf{f}} + \boldsymbol{n}\boldsymbol{p} + \hat{\boldsymbol{n}}\boldsymbol{q} \\ & F\left(\bar{\boldsymbol{\sigma}}_{\mathrm{n+1}}\right) \le 0 \\ & F_b\left(\boldsymbol{p},\ \boldsymbol{q}\right) \le 0 \end{aligned} \tag{28}$$

Obviously, this maximum problem is equivalent the following minimum problem:

$$\begin{aligned} \min_{\bar{\boldsymbol{\sigma}}_{\mathrm{n+1}},\,\boldsymbol{p},\,\boldsymbol{q}} \quad & \frac{1}{2}\Delta\bar{\boldsymbol{\sigma}}_{\mathrm{n+1}}^{\mathrm{T}}\mathbf{C}\Delta\bar{\boldsymbol{\sigma}}_{\mathrm{n+1}} + \sum_{I=1}^{N_b} g_0^I p^I \\ \text{subject to} \quad & \mathbf{B}^{\mathrm{T}}\bar{\boldsymbol{\sigma}}_{\mathrm{n+1}} = \tilde{\mathbf{f}} + \boldsymbol{n}\boldsymbol{p} + \hat{\boldsymbol{n}}\boldsymbol{q} \\ & F\left(\bar{\boldsymbol{\sigma}}_{\mathrm{n+1}}\right) \le 0 \\ & F_b\left(\boldsymbol{p},\ \boldsymbol{q}\right) \le 0 \end{aligned} \tag{29}$$

4. Second-order cone programming

The transformation of the optimisation problem (29) into a standard SOCP problem is explained in this section. Very efficient solvers capable of dealing with large-scale SOCP problems have been developed in last decades or so. Of particular notes are the packages MOSEK [13] and SeDuMi [14].

The SOCP is a generalisation of linear and quadratic programming that allows for affine combinations of variables to be constrained inside a special convex set, called second-order cone [45]. The following primal standard form of the SOCP is often used:

$$\begin{array}{ll} \min & \mathbf{a}^{\mathrm{T}} \boldsymbol{y} \\ \text{subject to} & \mathbf{D}\boldsymbol{y} = \boldsymbol{e} \\ & \boldsymbol{y} \in \mathcal{K} \end{array} \tag{30}$$

where $\boldsymbol{y}$ are the full problem variables and $\mathcal{K}$ is a Cartesian product of second-order cones i.e., $\mathcal{K} = \mathcal{K}_1 \times \mathcal{K}_2 \times \cdots \times \mathcal{K}_n$. Two most common conic cones are:

- the quadratic cone:

$$\mathcal{K}_q = \left\{ \boldsymbol{y} \in \mathbb{R}^m \mid y_1 \geq \sqrt{y_2^2 + \cdots + y_m^2} \right\} \tag{31}$$

- the rotated quadratic cone:

$$\mathcal{K}_r = \left\{ \boldsymbol{y} \in \mathbb{R}^m \mid 2y_1 y_2 \geq y_3^2 + \cdots + y_m^2, y_1 \geq 0,\ y_2 \geq 0 \right\} \tag{32}$$

Comparing (29) to the standard SOCP form (30), the quadratic term $\frac{1}{2}\Delta\bar{\boldsymbol{\sigma}}_{\mathrm{n+1}}^{\mathrm{T}}\mathbf{C}\Delta\bar{\boldsymbol{\sigma}}_{\mathrm{n+1}}$ in the objective function has to be removed. To this end, an auxiliary variable h is introduced in the objective function that is:

$$\begin{aligned}
&\min && \sum_{I=1}^{N_b} g_0^I p^I + h \\
&\text{subject to} && \mathbf{B}^{\mathrm{T}}\bar{\boldsymbol{\sigma}}_{\mathrm{n+1}} = \tilde{\mathbf{f}} + \boldsymbol{n}\boldsymbol{p} + \hat{\boldsymbol{n}}\boldsymbol{q} \\
& && h \geq \frac{1}{2}\Delta\bar{\boldsymbol{\sigma}}_{\mathrm{n+1}}^{\mathrm{T}}\mathbf{C}\Delta\bar{\boldsymbol{\sigma}}_{\mathrm{n+1}} \\
& && F\left(\bar{\boldsymbol{\sigma}}_{\mathrm{n+1}}\right) \leq 0 \\
& && F_b\left(\boldsymbol{p},\ \boldsymbol{q}\right) \leq 0
\end{aligned} \tag{33}$$

The newly introduced inequality constraint can be converted to a rotated quadratic cone:

$$\begin{aligned}
&\min && \sum_{I=1}^{N_b} g_0^I p^I + h \\
&\text{subject to} && \mathbf{B}^{\mathrm{T}}\bar{\boldsymbol{\sigma}}_{\mathrm{n+1}} = \tilde{\mathbf{f}} + \boldsymbol{n}\boldsymbol{p} + \hat{\boldsymbol{n}}\boldsymbol{q} \\
& && \boldsymbol{\xi}_{\bar{\sigma}} = \mathbf{C}^{\frac{1}{2}}\Delta\bar{\boldsymbol{\sigma}}_{\mathrm{n+1}},\ y_{\bar{\sigma}} = 1,\ (h, y_{\bar{\sigma}},\ \boldsymbol{\xi}_{\bar{\sigma}}) \in \mathcal{K}_r \\
& && \mathcal{K}_r = \left\{\ (h, y_{\bar{\sigma}},\ \boldsymbol{\xi}_{\bar{\sigma}}) \in \mathbb{R}^{m+2} \mid 2hy_{\bar{\sigma}} \geq \boldsymbol{\xi}_{\bar{\sigma}}^{\mathrm{T}}\boldsymbol{\xi}_{\bar{\sigma}},\ h \geq 0,\ y_{\bar{\sigma}} \geq 0\right\} \\
& && F\left(\bar{\boldsymbol{\sigma}}_{\mathrm{n+1}}\right) \leq 0 \\
& && F_b\left(\boldsymbol{p},\ \boldsymbol{q}\right) \leq 0
\end{aligned} \tag{34}$$

The yield criterion $F\left(\bar{\boldsymbol{\sigma}}_{\mathrm{n+1}}\right) \leq 0$ can be reformulated as a quadratic cone as well. Regarding the commonly used Mohr-Coulomb yield criterion, the following formulation applies to the plane strain problem:

$$F\left(\boldsymbol{\sigma}\right) = \sqrt{\left(\sigma_x - \sigma_y\right)^2 + 4\tau_{xy}^2} + \left(\sigma_x + \sigma_y\right)\sin\phi - 2c\cos\phi \leq 0 \tag{35}$$

Inequality (35) is reformulated as a quadratic cone that is:

$$\boldsymbol{\rho}_{n+1} = \begin{bmatrix} \rho_1 \\ \rho_2 \\ \rho_3 \end{bmatrix} \in \mathcal{K}_q,\ \mathcal{K}_q = \left\{ \boldsymbol{\rho}_{n+1} \in \mathbb{R}^3 \mid \rho_1 \geq \sqrt{\rho_2^2 + \rho_3^2} \right\} \tag{36}$$

where

$$\boldsymbol{\rho}_{n+1} = \mathbf{D}\boldsymbol{\sigma}_{\mathrm{n+1}} + \mathbf{d} = \begin{bmatrix} -\sin\phi & -\sin\phi & 0 \\ 1 & -1 & 0 \\ 0 & 0 & 2 \end{bmatrix} \begin{bmatrix} \sigma_x \\ \sigma_y \\ \tau_{xy} \end{bmatrix} + \begin{bmatrix} 2c\cos\phi \\ 0 \\ 0 \end{bmatrix} \tag{37}$$

It is necessary to note that other yield criteria such as the Drucker–Prager/von Mises model and the Cam-Clay model can be converted to second-order cones as well. Readers are referred to [12, 19, 46] for more details. In addition, multi-surface plasticity may be required for the model, which can be performed simply by adding more conic constraints in the optimisation problem.

The inequality constraint $F_b\left(\boldsymbol{p},\ \boldsymbol{q}\right) \leq 0$ owing to contacts has to be converted into a quadratic cone as well. This can be achieved by introducing a virtual shear strength $\overline{q}^I$ at each contact node *I* that is:

$$\begin{cases} \overline{q}^I = \mu p^I \geq \left| q^I \right|, & \text{frictional interfaces} \\ \overline{q}^I = \tan\phi p^I + cA^I \geq \left| q^I \right|, & \text{cohesive interfaces} \end{cases} \tag{38}$$

As a consequence, the related inequality constraint is reformulated as the following cone

$$\begin{gathered} \begin{bmatrix} \overline{q}^I \\ q^I \end{bmatrix} \in \mathcal{K}_q,\ I = 1,\ 2, \cdots,\ N_b \\ \mathcal{K}_q = \left\{ \left[\overline{q}^I,\ q^I \right]^{\mathrm{T}} \in \mathbb{R}^2 \mid \overline{q}^I \geq \sqrt{\left(q^I\right)^2} \right\} \end{gathered} \tag{39}$$

Finally, the SOCP problem equivalent to the minimisation problem (29) is as follows:

$$
\begin{aligned}
&\min \quad && \sum_{I=1}^{N_b} g_0^I p^I + h \\
&\text{subject to} \quad && \mathbf{B}^{\mathrm{T}}\bar{\boldsymbol{\sigma}}_{\mathrm{n+1}} = \tilde{\mathbf{f}} + \boldsymbol{n}\boldsymbol{p} + \hat{\boldsymbol{n}}\boldsymbol{q} \\
& && \boldsymbol{\xi}_{\bar{\sigma}} = \mathbf{C}^{\frac{1}{2}}\Delta\bar{\boldsymbol{\sigma}}_{\mathrm{n+1}},\ y_{\bar{\sigma}} = 1,\ (h, y_{\bar{\sigma}}, \boldsymbol{\xi}_{\bar{\sigma}}) \in \mathcal{K}_r \\
& && \mathcal{K}_r = \left\{ (h, y_{\bar{\sigma}}, \boldsymbol{\xi}_{\bar{\sigma}}) \in \mathbb{R}^{m+2} \mid 2hy_{\bar{\sigma}} \geq \boldsymbol{\xi}_{\bar{\sigma}}^{\mathrm{T}}\boldsymbol{\xi}_{\bar{\sigma}},\ h \geq 0,\ y_{\bar{\sigma}} \geq 0 \right\} \\
& && \boldsymbol{\rho}_{n+1} = \mathbf{D}\boldsymbol{\sigma}_{\mathrm{n+1}} + \mathbf{d} \\
& && \boldsymbol{\rho}_{n+1} \in \mathcal{K}_q,\ \mathcal{K}_q = \left\{ \boldsymbol{\rho}_{n+1} \in \mathbb{R}^3 \mid \rho_1 \geq \sqrt{\rho_2^2 + \rho_3^2} \right\} \\
& && \begin{bmatrix} \bar{q}^I \\ q^I \end{bmatrix} \in \mathcal{K}_q,\ I = 1,\ 2, \cdots,\ N_b \\
& && \mathcal{K}_q = \left\{ \left[\bar{q}^I,\ q^I\right]^{\mathrm{T}} \in \mathbb{R}^2 \mid \bar{q}^I \geq \sqrt{\left(q^I\right)^2} \right\}
\end{aligned}
\tag{40}
$$

In this work, MOSEK [13] is adopted as the SOCP solver.

5. Numerical examples

In this section, the correctness and robustness of the SOCP-SFEM is examined by modelling a series of benchmarks. The validation of the proposed approach in dealing with elastic problems and addressing the volumetric locking issues with linear elements is conducted in the first example. In the second example, the strip footing problem is adopted to validate the approach in modelling the associate and non-associated plasticity problems. The simulation results of the developed SOCP-SFEM are compared with analytical solutions and numerical results by the PLAXIS 2D software [47]. The bearing capacity can be derived with merely one loading step whereas more than 200 loading steps need to be used in PLAXIS. The robustness of the developed formulation for handling both the purely frictional contacts and cohesive-frictional contacts are shown in the third numerical example. In the last example, the unique feature of the approach (i.e., implementation of multi-surface plasticity models is no more involved than that of single-surface models) is demonstrated.

5.1 A plate with a central circular hole

To verify the developed formulation of the SOCP-SFEM, a quasi-static elastic boundary-value problem is concerned. The problem is shown in Fig. 3 [38] where an elastic plate with a central circular hole of radius *r*=1 m is subject to a horizontal tensile load σ_x = 1.0. The material parameters include an elastic module of 1.0 kPa and Poisson's ratio of 0.3. Only the upper right part is simulated owing to the symmetry and the domain is discretised using linear triangular elements as indicated in Fig. 3 (b). The analytical solutions of this plane-strain problem are available in [37, 48].

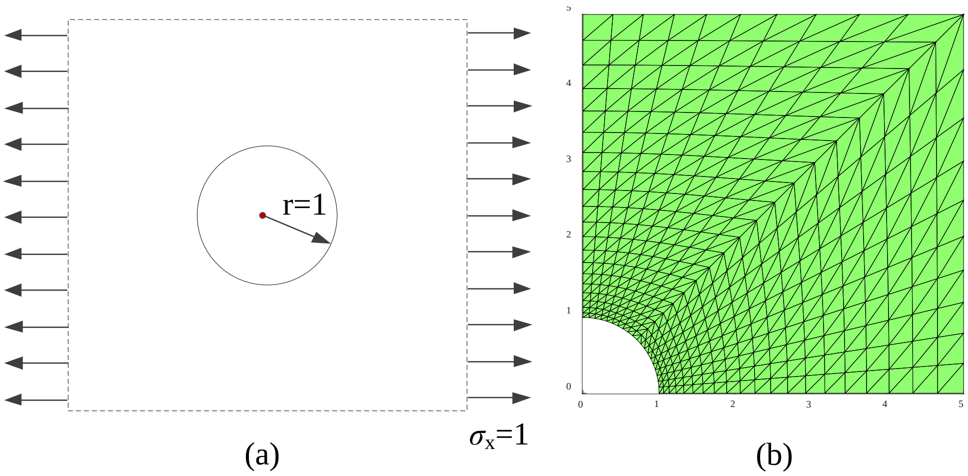

Fig. 3. The numerical model: (a) an infinite plate with a circular hole and (b) the discretised model using linear triangular elements (800 elements).

The SOCP-SFEM, the SFEM and the FEM method with linear elements are used to simulate this problem. One analysis step is conducted for this problem. Fig. 4 shows the displacement errors for three methods. It is observed that mesh refinement enhances the simulation accuracy. The numerical results of the SOCP-SFEM and the SFEM are identical, indicating the correctness of the developed SOCP-SFEM.

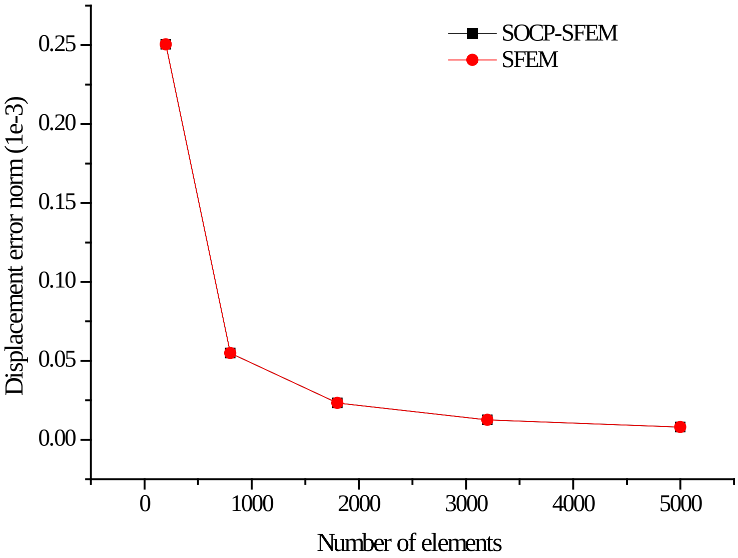

Fig. 4. Displacement error norm with different meshes.

Additionally, the well-known “overly stiff” phenomenon is studied using the developed approach. To this end, the problem is re-analysed with Poisson’s ratio increasing from 0.4 (for compressible materials) to 0.49999 (for incompressible materials). A total of 800 elements are used in the simulations. The corresponding displacement errors from different approaches for different Poisson’s ratios are shown in Fig. 5. The SFEM and the SOCP-SFEM lead to a very small error regardless of Poisson’s ratio, indicating that the SFEM and the SOCP-SFEM are naturally “immune” from the volumetric locking even though linear elements are used.

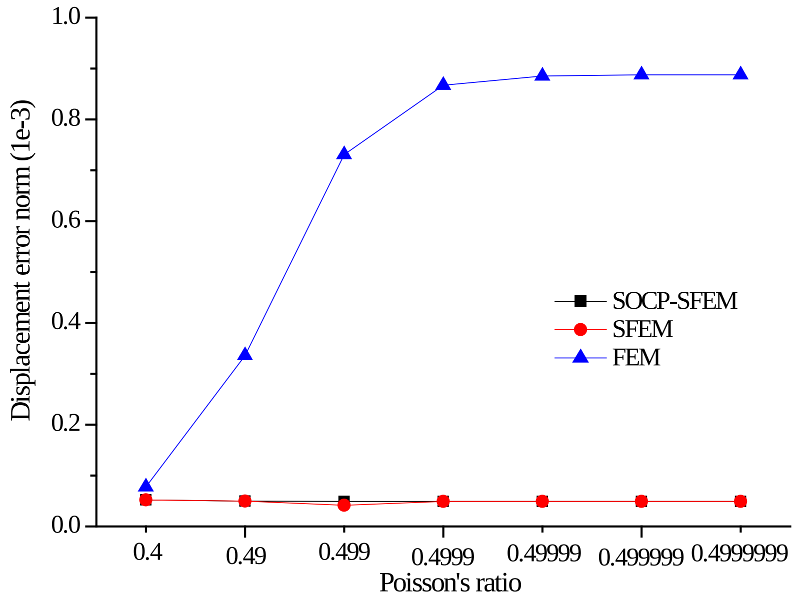

Fig. 5. Displacement errors with different Poisson's ratios (800 elements)

5.2 Strip footing

The classic bearing capacity problem of strip footing is concerned as the second example to test the SOCP-SFEM in modelling elastoplastic problems. The numerical model setup is shown in Fig. 6 where the domain is discretised using four different meshes from a very coarse one (184 elements) to a very fine one (20661 elements). The soil is assumed to be an elastic-perfectly plastic material with material parameters as follows: Young's modulus E = 100 MPa, Poisson's ratio υ = 0.49 and undrained shear strength S_u=100 kPa (Tresca model). The analysis is performed under the displacement control and the mobilised bearing capacity N_c is defined as:

$$N_c = \frac{F}{S_u B} \tag{41}$$

where F is the vertical reaction force on the footing.

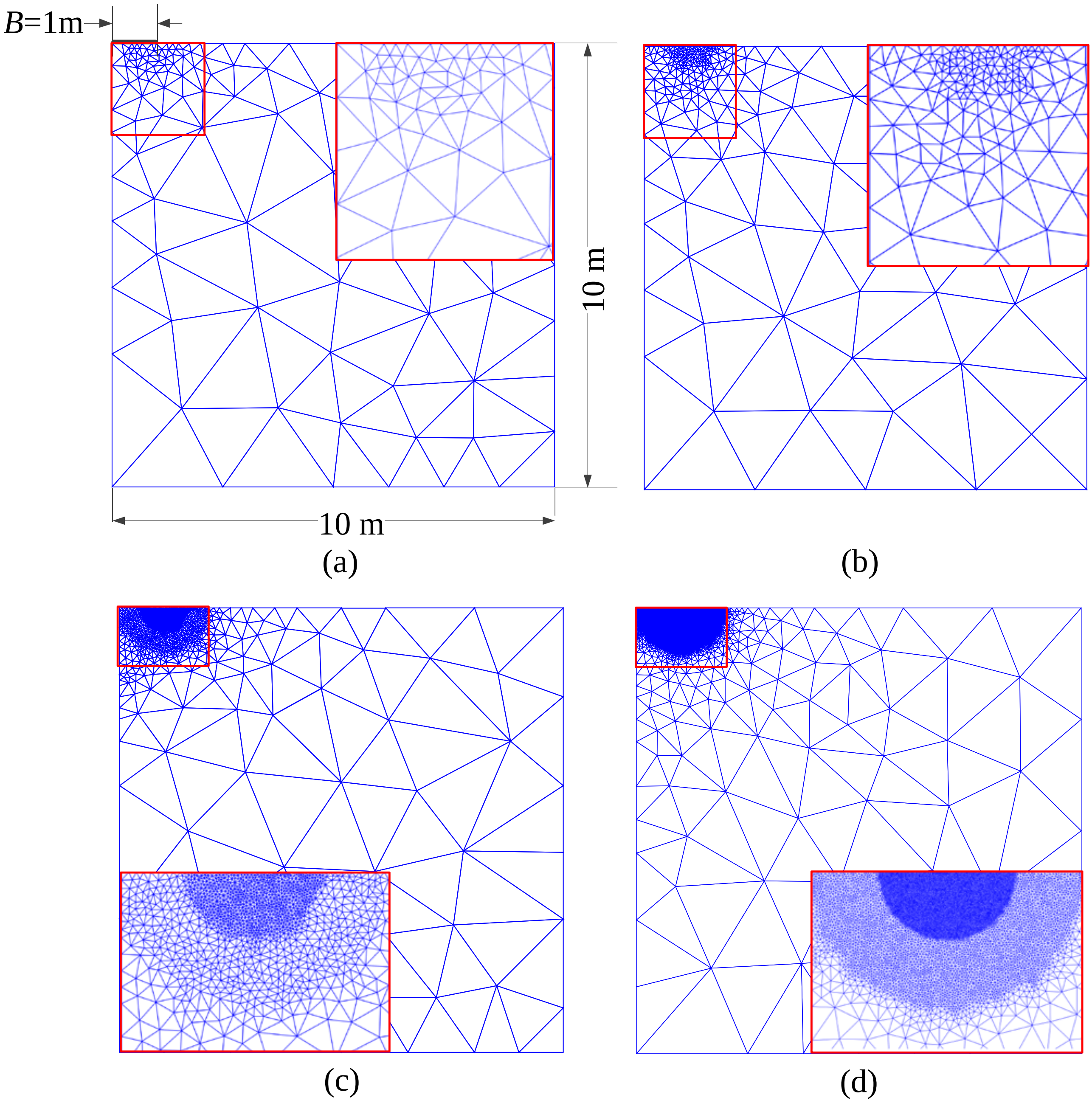

Fig. 6. Model setup with four finite element meshes: (a) 184 elements; (b) 390 elements; (c) 1144 elements and (d) 20661 elements.

For comparison purposes, the PLAXIS 2D software [47] is used. A total of 274 loading steps are implemented in the software to reach a vertical displacement of 0.2 m. The same loading process is used in our approach. The simulation results in comparison with the well-known Prandtl’s analytical solution (i.e. N_c=2+π) [49] are shown in Fig. 7. The results regarding the bearing capacities are summarised in Table 1. It shows a satisfactory agreement on the loading curves and bearing capacity even when a very coarse mesh is adopted.

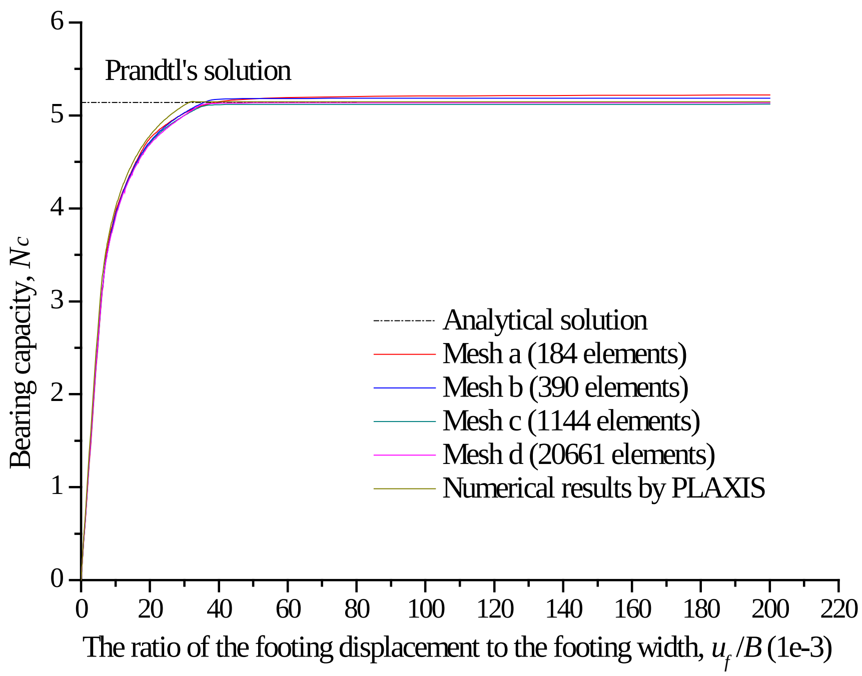

Fig. 7. Numerical load-displacement curves for the strip footing problem. The footing width and displacement are B and u_f, respectively.

Table 1. Bearing capacity with varied meshes

Meshes	Mesh a	Mesh b	Mesh c	Mesh d	PLAXIS
Bearing capacity, N_c	5.220	5.186	5.121	5.138	5.148
Relative error (%)	1.52	0.83	0.41	0.08	0.12

The influence of loading steps on the bearing capacity is studied. The loading steps ranging from 1, 10 to 100 are employed. The numerical results are shown in Fig. 8, in which numerical results of 274 loading steps from Table 1 are included. It shows loading steps have negligible impact on the bearing capacity. In other words, the bearing capacity can be estimated in only one step with the developed approach.

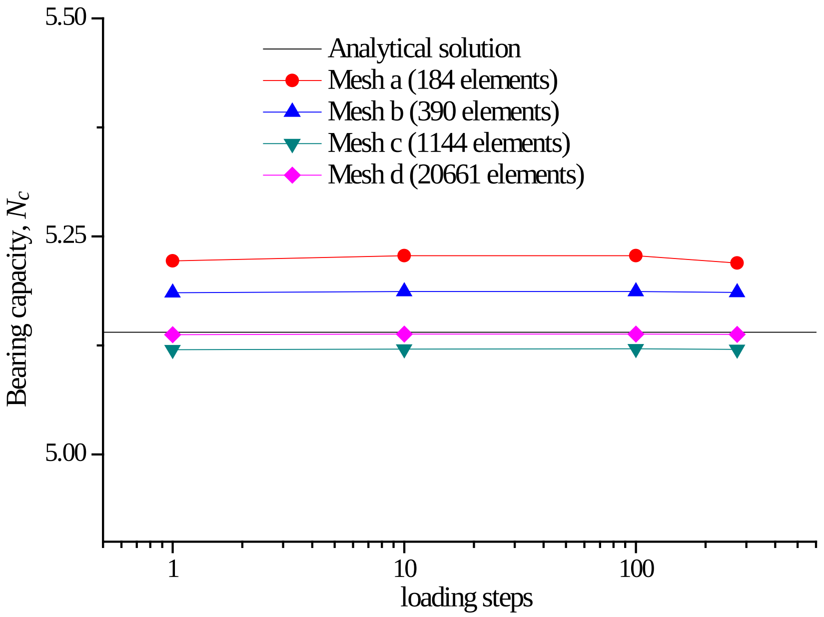

Fig. 8. Bearing capacity with varied loading steps.

Next, the soil is considered as a cohesive-frictional material. The setup of the problem is the same except that the Mohr-Coulomb yield criterion is applied. The frictional angle varies from 5˚ to 40˚ with an interval of 5˚ and the cohesion is 100 kPa. The mesh shown in Fig. 6 (d) is employed in this simulation. According to Prandtl's solution [49], the bearing capacity of the cohesive-frictional soil is:

$$N_c = (\tan^2\left(\frac{\pi}{4}+\frac{\phi}{2}\right)e^{\pi\tan\phi} - 1)\cot\phi \quad (42)$$

Fig. 9 shows the numerical results in comparison with those from Prandtl's solution where a good agreement is achieved.

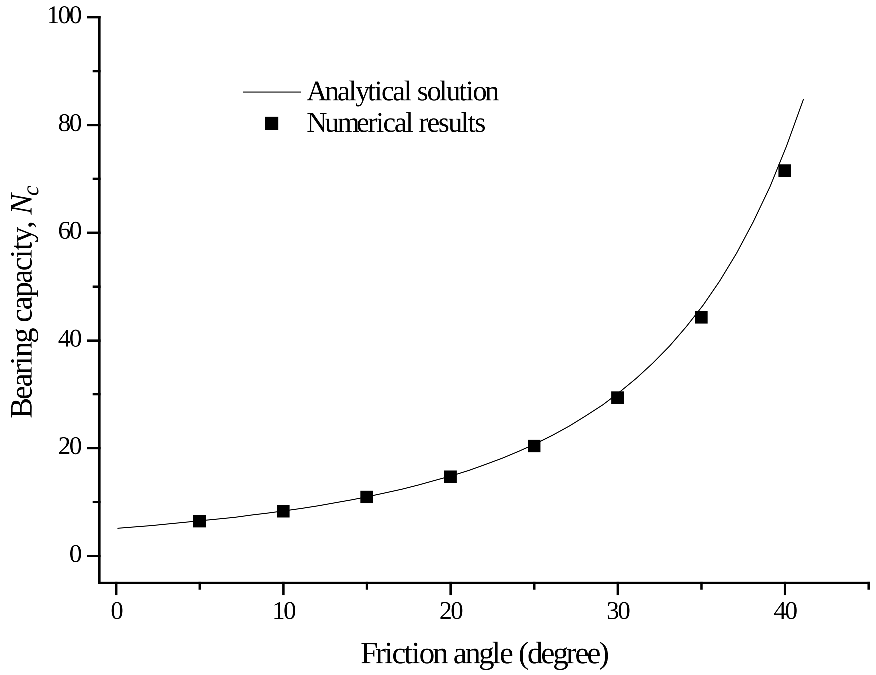

Fig. 9. Bearing capacity with varied friction angles

Although the associated flow rule is introduced in this approach, the computational associated scheme developed in [50, 51] can be employed, when modelling non-associated shear dilatancy. The basic operation is to replace the original yield function with an approximate function that coincides with the plastic potential at the current stress status. The model setup of the strip footing described above is employed here while the dilatancy angles are set as a third of the frictional angles. To test the results, the problem is conducted with the PLAXIS 2D software [47]. The numerical results by the proposed approach and PLAXIS are shown in Fig. 10. Their results reach a very good agreement. For the cases of the frictional angles of 35˚ and 40˚, PLAXIS suffers from numerical instabilities and an error code of 101 was reported. The possible reason is the nonuniqueness of the failure mechanism or a varying failure surface [52].

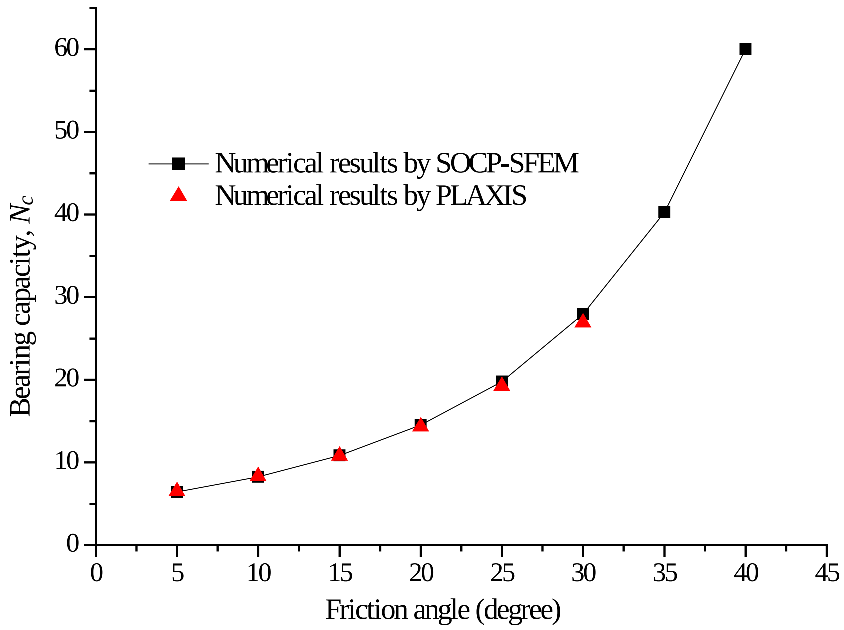

Fig. 10. Bearing capacity of the strip footing with the non-associated flow rule.

5.3 Cohesive-frictional contact behaviour

The interaction between a device and soils is of great importance for some geotechnical problems such as T-bar/cone penetrations, pipeline-soil interactions, and interactions between the sliding mass and the basal surface in landslides. The third numerical example is to show the capability of the developed formulation for handling both the purely frictional contacts and cohesive-frictional contacts. The numerical model is shown in Fig. 11 (a). Model parameters include length of rectangular blocks of 2 m, height of 1 m, density of 2.0×10^3 kg/m^3, elastic modulus of 100 MPa, Poisson’s ratio of 0.49 and gravitational acceleration of −9.8 m/s^2. Firstly, slope angle α is set to 0˚ for which an external force is required to move the block. For purely frictional interfaces, a series of frictional angles from 0˚ to 60˚ are used. For cohesive-frictional interfaces, the cohesion varies from 20 kPa, 50 kPa to 100 kPa. The external forces required to trigger the movement for all cases are recorded and compared to the analytical solution in Fig. 11 (b) where a good agreement has been achieved verifying the correctness of the developed frictional and cohesive-frictional contact formulation.

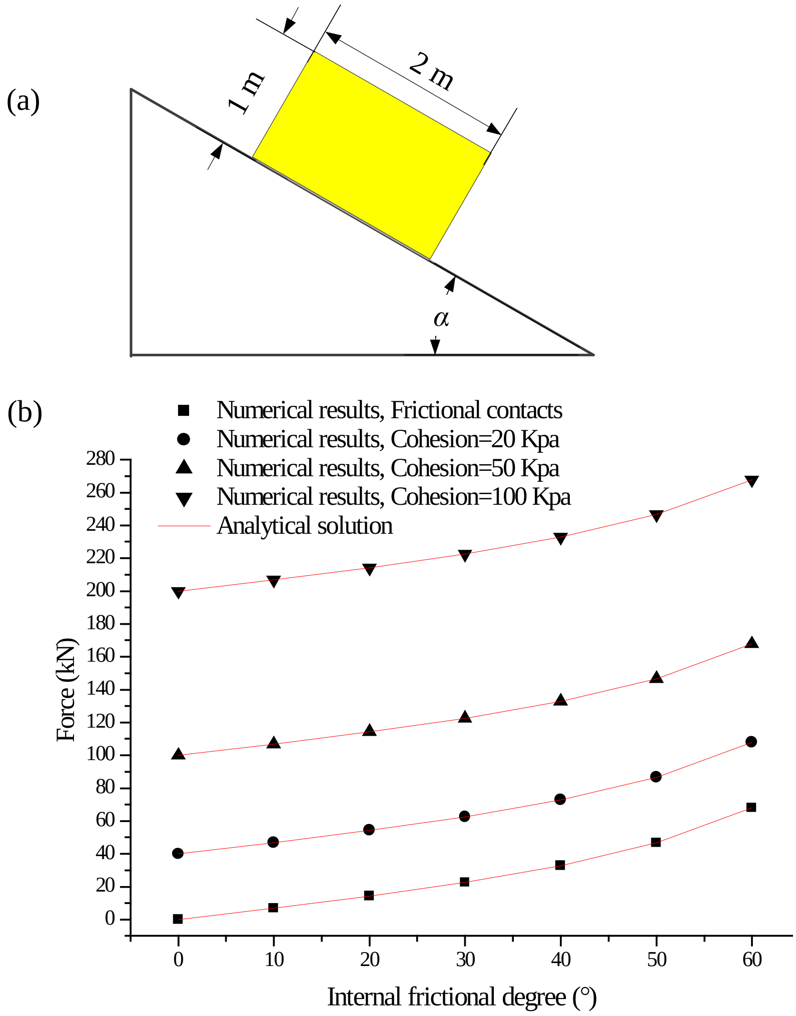

Fig. 11. The stability of a block: (a) geometric model and (b) comparison between numerical and analytical solutions, where α is the slope angle.

Next, a slope with a general angle (i.e. α=60˚) is considered to test contacts with an inclined surface. The internal frictional angle in this case decreases from 60˚ to 0˚. To maintain the stability of the block, a minimum cohesion is required. The numerical results in comparison with analytical solutions are shown in Fig. 12. As illustrated, the numerical results agree with the analytical solution, indicating the correctness of the improved contact formulations.

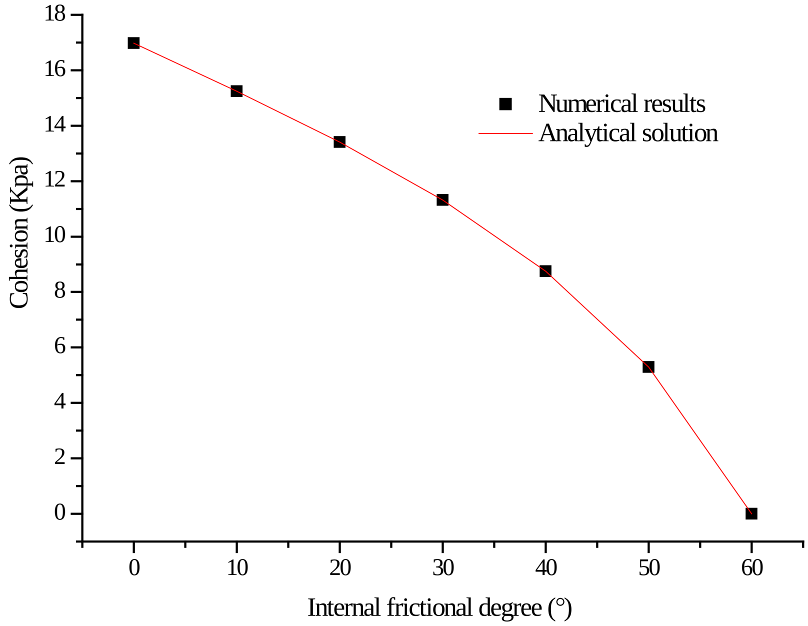

Fig. 12. A block resting on a slope

5.4 Bearing capacity of offshore pipelines

In this example, the proposed SOCP-SFEM is adopted to study the bearing capacity of a pipe embedded in undrained clays, which is a typical problem that should be considered in the design of pipeline networks. The problem setup is shown in Fig. 13. The major factors controlling the bearing capacity of the pipe include its embedment, the properties of the surrounding soil and the characteristics of the pipe/soil interface. In this study, the embedment of the pipeline is set to 5 m, the diameter of the pipe is D=1 m and the undrained shear strength of the soil is S_u=100 kPa. For simplicity, the soil is considered as weightless.

Four types of pipe surfaces are concerned as shown in Fig. 14. In reality, the surface can have the full shear strength of the soil, corresponding to the rough cases (for example, when the pipe is coated with rough concrete) or cannot resist any shear stress, i.e., the smooth cases (for example, when the pipe has a slippery plastic insulation coating). In addition, it is common to assume that the pipe surface cannot resist any tension (no tensile capacity) or the pipe surface is fully bonded (infinite tensile capacity). It is worth noting that, in our formulation, these requirements on the yield criterion of the pipe/soil interface cause little extra efforts.

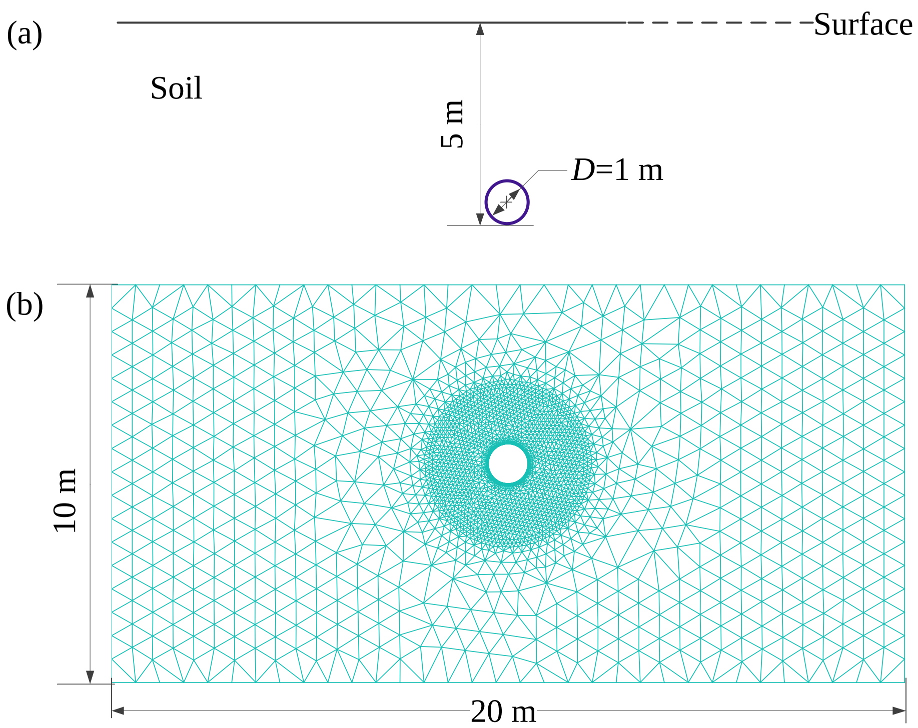

Fig. 13. The problem setup for a plane-strain pipe: (a) geometry and (b) mesh.

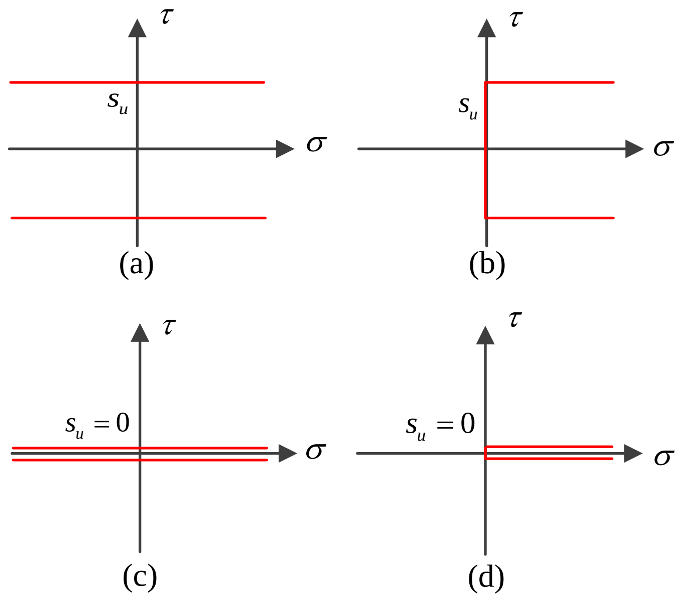

Fig. 14. Four soil-pipe interface models: (a) rough with tension, (b) rough without tension, (c) smooth with tension and (d) smooth without tension.

The numerical results of this problem using limit analysis are available in [53]. The penetration resistance P_r for all cases is calculated using our SOCP-SFEM in this study and compared to the limit analysis results from [53]. As shown in Fig. 15, a good agreement has been observed for two methods. Additionally, the failure mechanism of the clay for all cases is illustrated in Fig. 16 implying that the tensile strength plays a significant role on both the failure mechanism and the penetration resistance. The equivalent plastic strain increment is defined as $d\varepsilon_{eq}^{p}=\sqrt{2/3\left[\left(d\varepsilon_{x}^{p}\right)^{2}+\left(d\varepsilon_{y}^{p}\right)^{2}+2\left(d\varepsilon_{xy}^{p}\right)^{2}\right]}$ based on the von Mises criterion, where $d\varepsilon_{x}^{p}$ and $d\varepsilon_{y}^{p}$ are the normal plastic strain increments and $d\varepsilon_{xy}^{p}$ is the shear plastic strain increment.

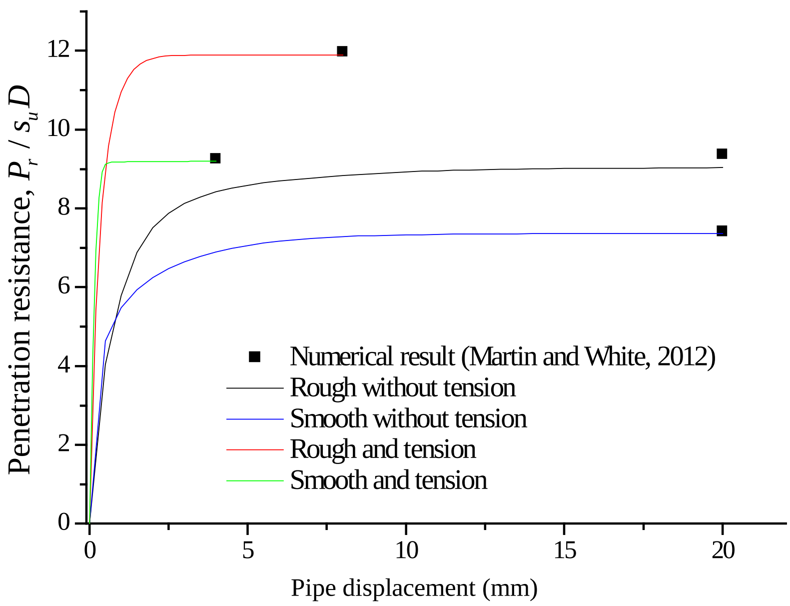

Fig. 15. Penetration resistance P_r for pipes in soils.

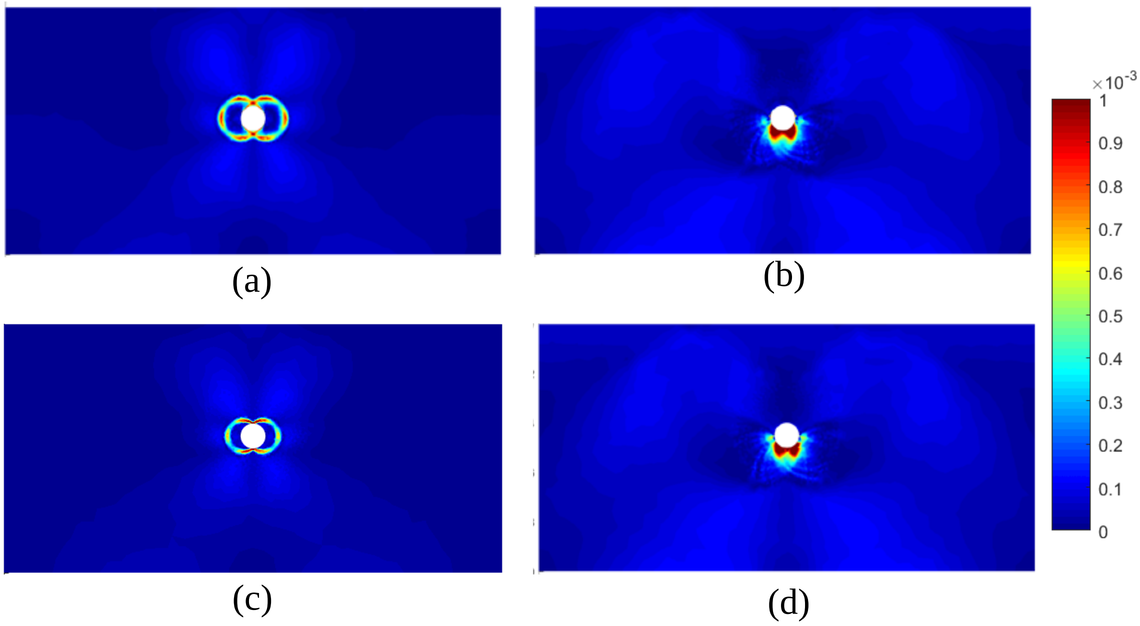

Fig. 16. Penetration mechanisms of four cases: (a) rough with tension, (b) rough without tension, (c) smooth with tension and (d) smooth without tension. Colours are proportional to the equivalent plastic strain increment.

6. Conclusion

In this paper, a finite element formulation called SOCP-SFEM is developed on the basis of the smoothed finite element method (SFEM) and the finite element method in second-order cone programing (SOCP-FEM). This is achieved by implementing the smoothing technique of the node-based SFEM into the computational framework of the SOCP-FEM. More specifically, the mixed variational principle is adopted to reformulate the elastoplastic boundary-value problem with contact interfaces into an equivalent min-max problem. The smoothed finite element discretisation is then performed to discretise the min-max problem with both the displacement and the smoothed stress being the independent fields which results in a uniform distribution of the strain and stress over the smoothing domain. The discretised min-max problem is then recast as a standard SOCP problem which is resolved using an efficient modern optimisation engine MOSEK.

Owing to the mixture, the SOCP-SFEM inherits the advantages of both the SOCP-FEM and the SFEM. The numerical examples show that linear elements can be used in the approach without special treatments for nearly incompressible materials since it is naturally immune from volumetric locking owing to the embedded strain smoothing technique. Additionally, since the final problem is in the form of a SOCP, it possesses advantages as follows: (1) the singularities in the Mohr-Coulomb and Drucker-Prager models can be treated naturally without approximations; (2) the extension from a single-surface yield function (e.g. cohesive interfaces) to a multi-surface yield function (e.g. cohesive interfaces with tension cut-off) is straightforward; and (3) the resulting SOCP problem can be resolved efficiently using the interior-point method available in advanced optimisation engine. Furthermore, the cohesive-frictional interface can be considered forthrightly owing to the use of smoothing domains.

It is also worth noting that, comparing to the SOCP-FEM, the developed SOCP-SFEM is more suitable to be implemented as the solver of the particle finite element method developed in [25] for large deformation analysis. This is because all variable states (e.g. displacements, strains and stresses) in the SOCP-SFEM are stored on mesh nodes, meaning that variable mapping from old meshes to new meshes is not required anymore in the particle finite element analysis of history-dependent problems despite remeshing operations.

Acknowledgement

The authors wish to acknowledge the support from the National Natural Science Foundation of China (Projects 51679117 and U1834206) and the Open Research Fund of State Key Laboratory of Coastal and Offshore Engineering, Dalian University of Technology (Project LP1926).

Notations

$\boldsymbol{A}$	cohesive interfaces' area
A_i^e	*i*th triangular element's area
A_k^s	area of the smoothing domain Ω_k^s
$\mathbf{b}$	body force
$\mathbf{B}_\mathrm{u}$ and $\mathbf{B}_i^e$	strain-displacement matrix and corresponding matrix of element i
$\overline{\mathbf{B}}_k$	smoothed strain-displacement matrix
$\mathbb{C}$	elastic compliance modulus
c	cohesion
D	diameter
E	elastic modulus
F	vertical loading
g_0^I and g^I	initial gap and contact gap at contact I
h, $\boldsymbol{\rho}_{n+1}$ and $\overline{q}^I$	auxiliary variables for standard SOCP program
$\boldsymbol{n}^I$, $\hat{\boldsymbol{n}}^I$	normal and shear vector at *I*th contact
$\boldsymbol{n}$ and $\hat{\boldsymbol{n}}$	matrices collecting the normal and tangential unit vectors
$\mathbf{N}$	matrix containing the unit outward normal to the boundary
N_c	bearing capacity for the strip footing problem
$\mathbf{N}_\mathrm{u}$ and $\mathbf{N}_\sigma$	matrix containing the shape functions for displacements and stresses
p^I and $\boldsymbol{p}$	normal contact force at contact I and its global vector
P_r	penetration resistance for the pipe

q^I and $\boldsymbol{q}$ tangential contact force at contact I and its global vector

$\overline{q}^I$ shear strength at contact I

r radius

s slack variable

S_u undrained shear strength

$\mathbf{t}$ tractions

$\mathbf{u}$ and $\hat{\mathbf{u}}$ displacement variable and nodes' displacement

$\hat{\mathbf{u}}_k$ and $\hat{\mathbf{u}}_i^e$ displacement in the smoothed domain k and the element i, respectively

$\Delta\hat{\mathbf{u}}^I$ and $\Delta\hat{\mathbf{u}}$ displacement increment at contact I and its global vector

α slope angle

$\Delta\boldsymbol{\varepsilon}$, $\Delta\boldsymbol{\varepsilon}^{\mathrm{e}}$ and $\Delta\boldsymbol{\varepsilon}^{\mathrm{p}}$ total strain increment, elastic part and plastic part

$\boldsymbol{\varepsilon}$ and $\boldsymbol{\varepsilon}_i^e$ strain and corresponding vector of element i

$\overline{\boldsymbol{\varepsilon}}_k$ smoothed strain in the smoothing domain Ω_k^s

λ Lagrange multiplier

μ friction coefficient

$\boldsymbol{\sigma}$ and $\overline{\boldsymbol{\sigma}}$ stress variables and smoothed stresses

υ Poisson's ratio

$\Phi_k(\mathbf{x})$ smoothing function

ϕ internal friction angle

References

[1] Sivaselvan M. Complementarity framework for non ‑ linear dynamic analysis of skeletal structures with softening plastic hinges. International Journal for Numerical Methods in Engineering. 2011;86(2):182-223.

[2] Sheng D, Sloan SW, Abbo AJ. An automatic Newton–Raphson scheme. The International Journal Geomechanics. 2002;2(4):471-502.

[3] Simo JC, Hughes TJ. Computational inelasticity. New York: Springer, 1998.

[4] Maier G. A matrix structural theory of piecewise linear elastoplasticity with interacting yield planes. Meccanica. 1970;5(1):54-66.

[5] Portioli F, Casapulla C, Cascini L. An efficient solution procedure for crushing failure in 3D limit analysis of masonry block structures with non-associative frictional joints. International Journal of Solids and Structures. 2015;69:252-66.

[6] Portioli F, Cascini L. Assessment of masonry structures subjected to foundation settlements using rigid block limit analysis. Engineering Structures. 2016;113:347-61.

[7] Makrodimopoulos A, Martin C. Lower bound limit analysis of cohesive ‑ frictional materials using second ‑ order cone programming. International Journal for Numerical Methods in Engineering. 2006;66(4):604-34.

[8] Le CV, Nguyen-Xuan H, Askes H, Rabczuk T, Nguyen-Thoi T. Computation of limit load using edge-based smoothed finite element method and second-order cone programming. International Journal of Computational Methods. 2013;10(01):1340004.

[9] Bolzon G, Maier G, Tin-Loi F. On multiplicity of solutions in quasi-brittle fracture computations. Computational Mechanics. 1997;19(6):511-6.

[10] Zhang X, Sheng D, Sloan SW, Bleyer J. Lagrangian modelling of large deformation induced by progressive failure of sensitive clays with elastoviscoplasticity. International Journal for Numerical Methods in Engineering. 2017;112(8):963-89.

[11] Krabbenhøft K, Lyamin A, Sloan S. Formulation and solution of some plasticity problems as conic programs. International Journal of Solids and Structures. 2007;44(5):1533-49.

[12] Makrodimopoulos A. Remarks on some properties of conic yield restrictions in limit analysis. International Journal for Numerical Methods in Biomedical Engineering. 2010;26(11):1449-61.

[13] Mosek A. The MOSEK optimization toolbox for MATLAB manual. Version 71 (Revision 28)2015.

[14] Sturm JF. Using SeDuMi 1.02, a MATLAB toolbox for optimization over symmetric cones. Optimization methods and software. 1999;11(1-4):625-53.

[15] Yonekura K, Kanno Y. Second-order cone programming with warm start for elastoplastic analysis with von Mises yield criterion. Optimization and Engineering. 2012;13(2):181-218.

[16] Wang D, Chen X, Lyu Y, Tang C. Geotechnical localization analysis based on Cosserat continuum theory and second-order cone programming optimized finite element method. Computers and Geotechnics. 2019;114:103118.

[17] Bleyer J, Maillard M, De Buhan P, Coussot P. Efficient numerical computations of yield stress fluid flows using second-order cone programming. Computer Methods in Applied Mechanics and Engineering. 2015;283:599-614.

[18] Bleyer J. Advances in the simulation of viscoplastic fluid flows using interior-point methods. Computer Methods in Applied Mechanics and Engineering. 2018;330:368-94.

[19] Zhang X, Sheng D, Sloan SW, Krabbenhoft K. Second-order cone programming formulation for consolidation analysis of saturated porous media. Computational Mechanics. 2016;58(1):29-43.

[20] Zhang X, Sloan SW, Oñate E. Dynamic modelling of retrogressive landslides with emphasis on the role of clay sensitivity. International Journal for Numerical and Analytical Methods in Geomechanics. 2018;42(15):1806-22.

[21] Huang J, da Silva MV, Krabbenhoft K. Three-dimensional granular contact dynamics with rolling resistance. Computers and Geotechnics. 2013;49:289-98.

[22] Krabbenhoft K, Huang J, Da Silva MV, Lyamin A. Granular contact dynamics with particle elasticity. Granular Matter. 2012;14(5):607-19.

[23] Krabbenhoft K, Lyamin A, Huang J, da Silva MV. Granular contact dynamics using mathematical programming methods. Computers and Geotechnics. 2012;43:165-76.

[24] Meng J, Huang J, Sheng D, Sloan SW. Granular contact dynamics with elastic bond model. Acta Geotechnica. 2017;12(3):479-93.

[25] Zhang X, Krabbenhoft K, Pedroso D, Lyamin A, Sheng D, Da Silva MV, et al. Particle finite element analysis of large deformation and granular flow problems. Computers and Geotechnics. 2013;54:133-42.

[26] Zhang X, Krabbenhoft K, Sheng D, Li W. Numerical simulation of a flow-like landslide using the particle finite element method. Computational Mechanics. 2015;55(1):167-77.

[27] Zhang X, Krabbenhoft K, Sheng D. Particle finite element analysis of the granular column collapse problem. Granular Matter. 2014;16(4):609-19.

[28] Meng J, Cao P, Huang J, Lin H, Chen Y, Cao R. Second-order cone programming formulation of discontinuous deformation analysis. International Journal for Numerical Methods in Engineering. 2019;118(5):243-57.

[29] Meng J, Cao P, Huang J, Lin H, Li K, Cao R. Three-dimensional spherical discontinuous deformation analysis using second-order cone programming. Computers and Geotechnics. 2019;112:319-28.

[30] Meng J, Huang J, Lin H, Laue J, Li K. A static discrete element method with discontinuous deformation analysis. International Journal for Numerical Methods in Engineering. 2019;120(7):918-35.

[31] Portioli F, Cascini L. Large displacement analysis of dry-jointed masonry structures subjected to settlements using rigid block modelling. Engineering Structures. 2017;148:485-96.

[32] Portioli F, Cascini L. Contact dynamics of masonry block structures using mathematical programming. Journal of Earthquake Engineering. 2018;22(1):94-125.

[33] Meng J, Huang J, Sloan S, Sheng D. Discrete modelling jointed rock slopes using mathematical programming methods. Computers and Geotechnics. 2018;96:189-202.

[34] Meng J, Huang J, Yao C, Sheng D. A discrete numerical method for brittle rocks using mathematical programming. Acta Geotechnica. 2018;13:283-302.

[35] Zhang X, Oñate E, Torres SAG, Bleyer J, Krabbenhoft K. A unified Lagrangian formulation for solid and fluid dynamics and its possibility for modelling submarine landslides and their consequences. Computer Methods in Applied Mechanics and Engineering. 2019;343:314-38.

[36] Zeng W, Liu G. Smoothed finite element methods (S-FEM): an overview and recent developments. Archives of Computational Methods in Engineering. 2018;25(2):397-435.

[37] Liu G-R, Trung N. Smoothed finite element methods. 6000 Broken Sound Parkway NW, Suite 300: CRC press, 2010.

[38] Liu G, Nguyen-Thoi T, Nguyen-Xuan H, Lam K. A node-based smoothed finite element method (NS-FEM) for upper bound solutions to solid mechanics problems. Computers & structures. 2009;87(1-2):14-26.

[39] Nguyen-Thoi T, Vu-Do H, Rabczuk T, Nguyen-Xuan H. A node-based smoothed finite element method (NS-FEM) for upper bound solution to visco-elastoplastic analyses of solids using triangular and tetrahedral meshes. Computer Methods in Applied Mechanics and Engineering. 2010;199(45-48):3005-27.

[40] Nguyen‐Xuan H, Bordas S, Nguyen‐Dang H. Smooth finite element methods: convergence, accuracy and properties. International Journal for Numerical Methods in Engineering. 2008;74(2):175-208.

[41] Reissner E. On a variational theorem in elasticity. Journal of Mathematics and Physics. 1950;29(1-4):90-5.

[42] Boyd S, Vandenberghe L. Convex optimization: Cambridge university press, 2004.

[43] Krabbenhoft K, Lyamin AV, Hjiaj M, Sloan SW. A new discontinuous upper bound limit analysis formulation. International Journal for Numerical Methods in Engineering. 2005;63(7):1069-88.

[44] Vanderbei RJ. Linear programming: Foundations and extensions. International Series in Operations Research & Management Science, 37. Kluwer Academic Publishers, Boston, MA, 2001.

[45] Calafiore GC, Ghaoui LE. Optimization models: Cambridge University Press, 2014.

[46] Krabbenhoft K, Lyamin A. Computational Cam clay plasticity using second-order cone programming. Computer Methods in Applied Mechanics and Engineering. 2012;209:239-49.

[47] Brinkgreve R, Swolfs W, Engin E, Waterman D, Chesaru A, Bonnier P, et al. PLAXIS 2D 2010. User manual, Plaxis bv. 2010.

[48] Timoshenko S, Goodier J. "Theory of Elasticity," 3rd Edition. New York: McGraw Hill, 1970.

[49] Terzaghi K, Peck R. Soil Mechanics in Engineering Practice. 2nd Edition. New York: John Wiley, 1967.

[50] Krabbenhoft K, Karim M, Lyamin A, Sloan S. Associated computational plasticity schemes for nonassociated frictional materials. International Journal for Numerical Methods in Engineering. 2012;90(9):1089-117.

[51] Chen X, Wang D, Yu Y, Lyu Y. A modified Davis approach for geotechnical stability analysis involving non-associated soil plasticity. Géotechnique. 2020;0(0):1-11.

[52] Lin H-D, Wang W-C, Li A-J. Investigation of dilatancy angle effects on slope stability using the 3D finite element method strength reduction technique. Computers and Geotechnics. 2020;118:103295.

[53] Martin C, White D. Limit analysis of the undrained bearing capacity of offshore pipelines. Géotechnique. 2012;62(9):847.